

# High-Resolution Volumetric Imaging and Classification of Organisms with Standard Optical Microscopy

Yaoran Liu, Rohit Unni, Xin Lou, Mingcheng Yang, and Yuebing Zheng\*



Cite This: *Nano Lett.* 2023, 23, 5148–5154



Read Online

ACCESS |



Metrics & More



Article Recommendations

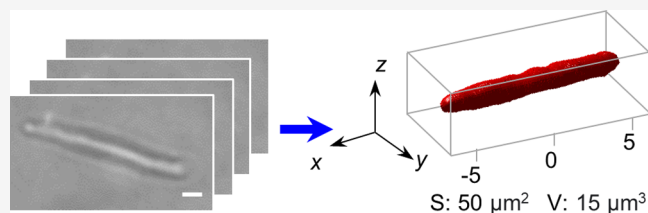


Supporting Information

**ABSTRACT:** Three-dimensional (3D) characterization of organisms is important for the study of cellular phenotypes, structural organization, and mechanotransduction. Existing optical techniques for 3D imaging rely on focus stacking or complex multiangle projection. Focus stacking has deleterious axial resolution due to the one-angle optical projection. Herein, we achieve high-resolution 3D imaging and classification of organisms based on standard optical microscopy coupled to optothermal rotation.

Through a seamless fusion of optical trapping and rotation of organisms on a single platform, our technique is applicable to any organism suspended in clinical samples, enabling contact-free and biocompatible 3D imaging. Moreover, when applying deep learning to distinguish different types of biological cells with high similarity, we demonstrate that our platform improves the classification accuracy (96% vs 85%) while using one-tenth the number of training samples compared with conventional deep-learning-based classification.

**KEYWORDS:** optical tweezer, cell imaging, thermophoresis, machine learning, optical rotation



Analysis and visualization of three-dimensional (3D) properties of cells and organisms are of fundamental importance for the understanding of cell lineage and communication networks.<sup>1,2</sup> Volumetric imaging of single organisms can be acquired through the form of a focal stack by taking sequential images in tens to hundreds of two-dimensional focal planes. Despite high lateral resolution ( $x$  axis), the optical sectioning along a single axis causes missing cones in optical transfer function and low axial resolution (over  $1 \mu\text{m}$ ) along the  $z$  axis, which is insufficient to resolve subcellular phenomena<sup>3</sup> (Figure 1a). Other emerging optical imaging systems such as selective plane illumination microscopy<sup>4</sup> (SPIM) and total internal reflection fluorescence<sup>5</sup> only allow a small portion of the sample that is close to the objectives to be imaged at high resolution.<sup>5,6</sup> Recently, multiview SPIM has been developed to reduce the deleterious effects of optical shadowing, occlusion, and scattering by adding more objectives to view the specimen from multiple directions, which improves the axial resolution and overall 3D imaging resolution.<sup>7,8</sup> However, adding more objectives still cannot provide full  $360^\circ$  optical imaging with high resolution (Figure 1b).

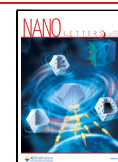
Continuously rotating the sample can achieve full  $360^\circ$  optical imaging with a standard optical microscope<sup>9,10</sup> (Figure 1c). Achieving multiple views of the specimen is equivalent to rotating the optical transfer function in 3D. Therefore, the sample rotation resolves the missing cone issue along the  $z$  axis in a conventional wide-field microscope while providing the finer features. However, the most common methods for sample rotation require high hardware precision and stability along

with cells being fixed on the substrate.<sup>5</sup> Emerging sample rotation by external fields (i.e., optical, acoustic, and magnetic) is contact-free, cell-friendly, and easy to integrate with microfluidic devices. These field-based manipulation techniques exhibit their best performances in certain applications.<sup>11,12</sup> Acoustic tweezers are most suitable for large organisms and have difficulty in handling single cells with their sizes smaller than the ultrasound wavelength.<sup>13–15</sup> Optical tweezers have a better control on cells with their sizes ranging from the nanoscale to microscale when using a tightly focused laser beam with a wavelength of  $<1 \mu\text{m}$ .<sup>16</sup> Optical tweezers have been applied for 3D manipulation of colloidal nanoparticles, cells, and proteins.<sup>17–21</sup> Precise control of the orientation of colloidal nanoparticles can be achieved based on the predictable optical forces and the corresponding motion of samples,<sup>22</sup> providing tomographic characterization down to the single-molecule level.<sup>23,24</sup> However, conventional optical trapping cannot achieve a stable rotation of organisms with high asymmetry and mobility due to their unpredictable shapes and optical properties, resulting in inaccurate imaging with optical microscopy<sup>25,26</sup> (Figure 1d). Meanwhile, excellent

Received: March 21, 2023

Revised: May 16, 2023

Published: May 30, 2023



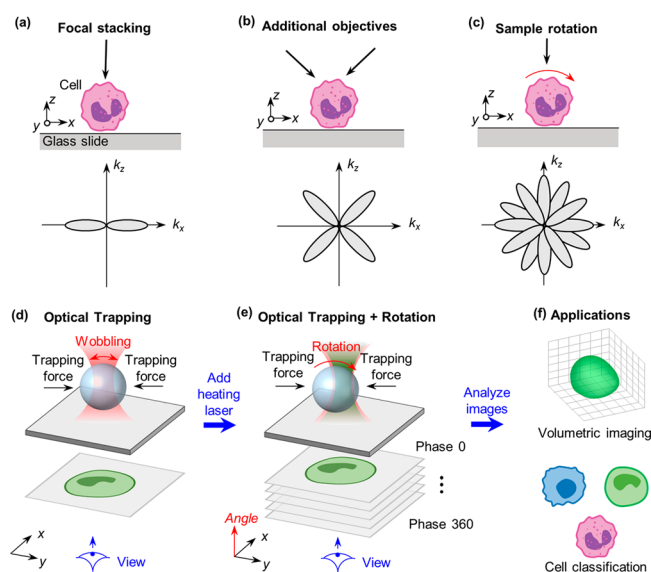


**Figure 1.** Illustration of volumetric imaging of cells using different techniques and our optical trapping and rotation method for enhanced cell imaging and classification. (a) Top panel: schematic showing the conventional focal stacking for cell imaging. Bottom panel: optical transfer function of the cell imaging. (b) Top panel: schematic showing the cell imaging by adding more objectives. Bottom panel: optical transfer function of the cell imaging. (c) Top panel: schematic showing the cell imaging with sample rotation. Bottom panel: optical transfer function of the cell imaging. (d) In conventional optical trapping, the optical force traps the object at the center of the laser beam where the cell asymmetry induces wobbling. As a result, the image is typically captured from the cell with a random orientation, causing the imaging inaccuracy. (e) By adding a heating laser, we achieve optical rotation of the trapped cell, which allows multiangle projection imaging in deterministic angles. (f) A series of planar images of a rotating cell can be stacked to provide volumetric information on the cell. The cell images at the variable rotating states enable us to train ML to achieve a more accurate cell classification with small sample quantities. The black arrows in (a)–(c) indicate the light propagation direction.

work on cell rotation through hydrodynamic flows has been reported.<sup>27–29</sup>

To enhance volumetric imaging and classification of organisms with conventional optical microscopy, we develop a universal optothermal rotation technique integrated with an optical microscope. Different from conventional optical rotation requiring specific shapes and optical properties of the target objects, our technique exploits optothermally generated osmotic force from a heating laser to drive the rotation of an arbitrary organism (Figure 1e). Since we can achieve out-of-plane rotation by simply adding another laser beam without using bulky microfluidic pumps and tubes, our technique shows several advantages in terms of the size, cost, throughput, and sample volume over conventional hydrodynamic rotation (Supporting Text 1). To further facilitate 3D imaging, we achieve out-of-plane rotation of organisms around the direction orthogonal to the laser beam propagation direction.<sup>30</sup> The stable out-of-plane rotation of organisms provides multiangle projection imaging stacking and *in situ* volumetric visualization with an overall 3D resolution of 85 nm approaching the lateral resolution of the parent microscopy (Figure 1f). We have demonstrated volumetric imaging for a wide range of organisms from nanometer-scale bacteria to micrometer-scale neutrophils and cells in clinical samples.

Furthermore, we apply a machine learning (ML) method to enhance classification of organisms based on their volumetric images. ML has rapidly developed into a powerful tool for interpreting and differentiating cell images.<sup>31–35</sup> However, the high economic and time cost required to acquire sufficiently sized high-quality data sets remains a significant bottleneck for ML in many applications.<sup>36</sup> When applied to the cell classification between pathogenic and nonpathogenic cells, our multiangle projection imaging enabled by the optical out-of-plane rotation allows the collection of large numbers of unique images for each cell, improving the cell classification accuracy (96% vs 85%) while using one-tenth the number of samples for the ML training (Figure 1f). Accordingly, we can easily detect rare and barely distinguishable pathogenic cells in the clinical samples and trap the target cells for single-cell analysis based on a simple optical microscope.

The experimental setup and working principle of our optothermal rotation, which is universally applicable to various organisms, are illustrated in Figure 2a. The substrate is a transparent Au thin film with a thickness of 4.5 nm. Two laser beams with wavelengths of 785 and 532 nm are focused on a heating substrate, and the real-time optical images of the cell are collected using a high-speed CMOS camera. Specifically, a 785 nm laser with an intensity of 1 mW/ $\mu\text{m}^2$  and beam diameter of 2  $\mu\text{m}$  is used to trap the cell with optical forces. The absorption of our substrate near 785 nm is low,<sup>37</sup> and therefore the heating effect from the 785 nm laser can be ignored (Figure S1). The distance between the cell and the substrate can be precisely adjusted by moving the z axis through the 785 nm laser. The 532 nm laser with an intensity of 0.6 mW/ $\mu\text{m}^2$  and beam diameter of 1  $\mu\text{m}$  is used to heat the light-absorbing substrate near the trapped cell to create a temperature gradient field (Figure 2b), generating thermophoretic force and thermo-osmotic force that repel and trap the cell, respectively.<sup>38,39</sup> Thermo-osmosis is a surface-driven effect that is parallel to the substrate where its slip velocity decreases with the increasing distance to the heating center.<sup>40,41</sup> We simulated the flow profile around a suspended hard sphere with a diameter of 5  $\mu\text{m}$  under the temperature gradient (Figure 2c).<sup>42</sup> The thermo-osmotic force generates an unbalanced flow along the sphere surface and exerts a torque on the trapped sphere for its stable rotation. The rotation is anticlockwise when a cell is trapped at the left side of the laser beam, and vice versa. It should be noted that the osmotic velocity decreases with increasing distance between the substrate and the cell, and therefore the rotational speed also decreases. As a demonstration, Figure 2d shows the successive images of light-driven trapping and rotation of a single bacterium above a substrate (movie S1). As shown in movie S2, once the cell gets trapped by the laser and rotation starts, the rotating cell will remain at the trapping center and the rotational speed stays the same without escape for over 90 s. To further verify the proposed mechanism for optothermal manipulation, we tracked the central position of a cell being trapped and rotated relative to the laser beam center. The temporal trajectory distribution of the cell center shows that the stable cell-trapping position is away from the laser center (0, 0) and the cell moves around the laser beam (Figures 2e,f), which matches well with our force analysis (Figure S2). Since the thermo-osmotic flow increases monotonically with the laser power, a linear relation between rotational speed and heating laser power further indicates that the rotation is mainly contributed by the thermo-osmotic flow. It should be noted

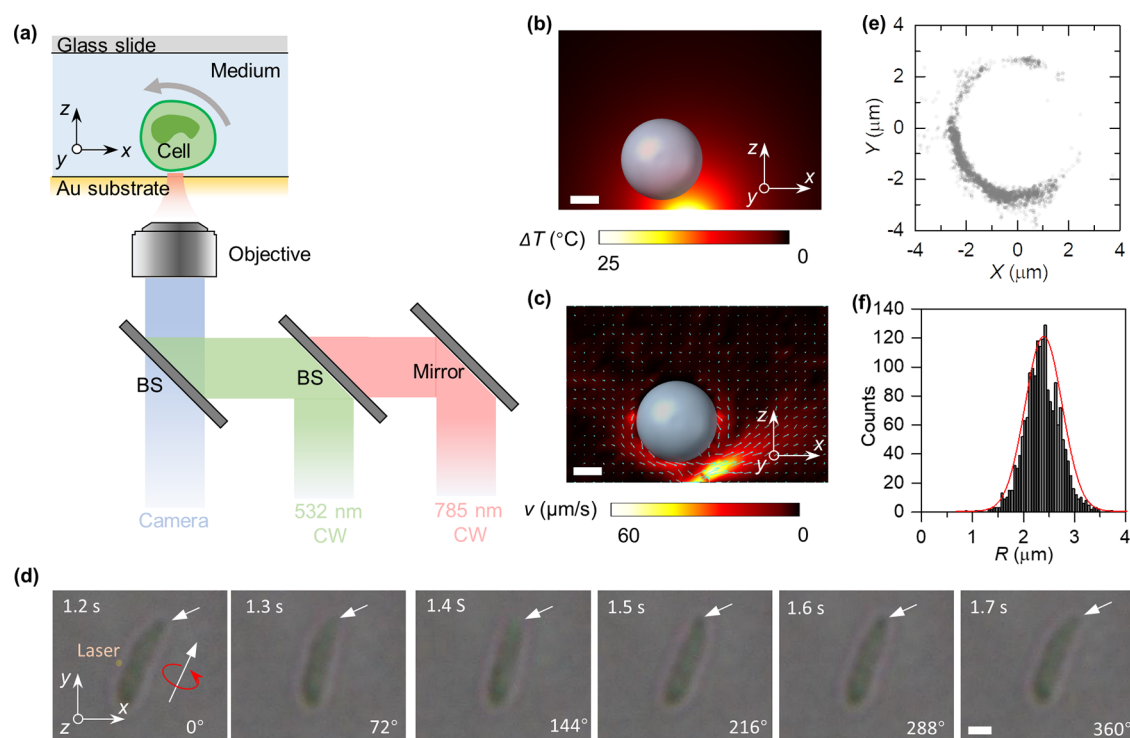


**Figure 2.** Working principle of optical trapping and rotation. (a) Experimental setup to achieve optical trapping and rotation. BS denotes a beam splitter. CW denotes a continuous wave. (b) Temperature profile at the focal plane. The 532 nm laser intensity is  $0.6 \text{ mW}/\mu\text{m}^2$ . (c) The flow profile around the trapped objects with a diameter of  $5 \mu\text{m}$ . (d) Image sequence showing a cycle of rotational bacteria. The arrow highlights the changing features at each orientation angle. (e) A temporal trajectory in  $x$ - $y$  plane of the center of a rotating cell relative to the laser beam center (0, 0). (f) Histogram with Gaussian fitting of the radial distance from the cell center to the laser beam center. Scale bars in (b) and (c):  $2 \mu\text{m}$ .

that, while the heating laser might reduce the cell viability, the distance between the heating center and the trapped cell center is over  $2 \mu\text{m}$  due to the repelling thermophoretic force and the actual temperature on the cell membrane is approximately  $37 \text{ }^\circ\text{C}$  when the laser power is  $0.6 \text{ mW}/\mu\text{m}^2$ , which causes no damage to the cell (Figure 2b).

To demonstrate the general capability of our optical rotation, we took human clinical samples (i.e., blood and urine), which contain different cells with a variety of shapes and sizes (Figure 3a). We injected separated blood and native urine into a microfluidic channel and identified our targeted organisms under an optical microscope (see Materials and Methods in the Supporting Information). Continuous rotation of a wide range of organisms is achieved in human urine and blood (Figure S3 and movie S3). The rotation stops immediately once we turn off the laser beam. With the same laser power, the rotational speed is different for organisms with different sizes. We also achieved optical rotation of a small organism with a size of  $500 \text{ nm} \times 300 \text{ nm}$  (Figure S4). To retrieve the rotation behaviors of a diffraction-limited organism, we collected the time-dependent total light intensity signals of the trapped cell and the time-dependent oscillatory intensity of the optical images corresponding to its continuous rotation with a rotational speed of  $\sim 1.5 \text{ Hz}$  (Figure S4). For the smaller organisms, the imaging quality for the rotation becomes poor. However, it should be noted that, since our rotation is based on the localized fluidic flow rather than the optical torque, rotation of a small organism with its size below the diffraction limit of light is still feasible.

Multangle projection imaging based on optical rotation leads to tomographic architectures of cells with high lateral resolution. As a demonstration, we recorded a series of optical

images of rotating bacterium, neutrophil, and fungus (Figure 3b–d). The cell contour images were extracted from the raw images. To eliminate the noise in contour points, we took 5–6 rounds of rotational images and generated a point cloud with 3D coordinates, from which 3D surface consisting of optimized triangles was constructed (movies S4–S6). To retrieve the 3D surface of a bacterium, we collected the rotational images at an interval of 10 rotational degrees, which corresponds to approximately 85 nm resolution for a bacterium with a diameter of  $\sim 1 \mu\text{m}$  along its rotational axis. For small organisms with a high rotational rate, the tomographic reconstruction rates can reach 2 Hz, allowing high-speed real-time tomographic visualization of the trapped organisms. It should be noted that the current acquisition rate is limited by the camera frame rate ( $\sim 50 \text{ Hz}$ ), which can be enhanced by using a high-speed camera (1 kHz frame rate). From the retrieved 3D surface, a variety of biological information can be obtained for the organism. For example, the surface area and volume of the bacterium are  $50 \mu\text{m}^2$  and  $15 \mu\text{m}^3$ , respectively, while the neutrophil shows a larger surface area and volume with values of  $687 \mu\text{m}^2$  and  $803 \mu\text{m}^3$ , respectively. From *in situ* volumetric imaging, we can clearly observe the locally curved shape on the bacterium membrane. Compared with the bacterium, the neutrophil exhibits a rougher surface with microvilli and tethers nonuniformly distributed on its surface. We further conducted the intracellular imaging using quantitative phase imaging camera (SID4-Bio, PHASCIS). We acquired 2D quantitative phase images of a rotating cell and retrieved the refractive index (RI) imaging.<sup>27</sup> As shown in Figure 4, we achieved RI mapping of a yeast cell at different rotation angles. We can observe a clear high RI region that corresponds to the nucleus. Owing to the reduced optical

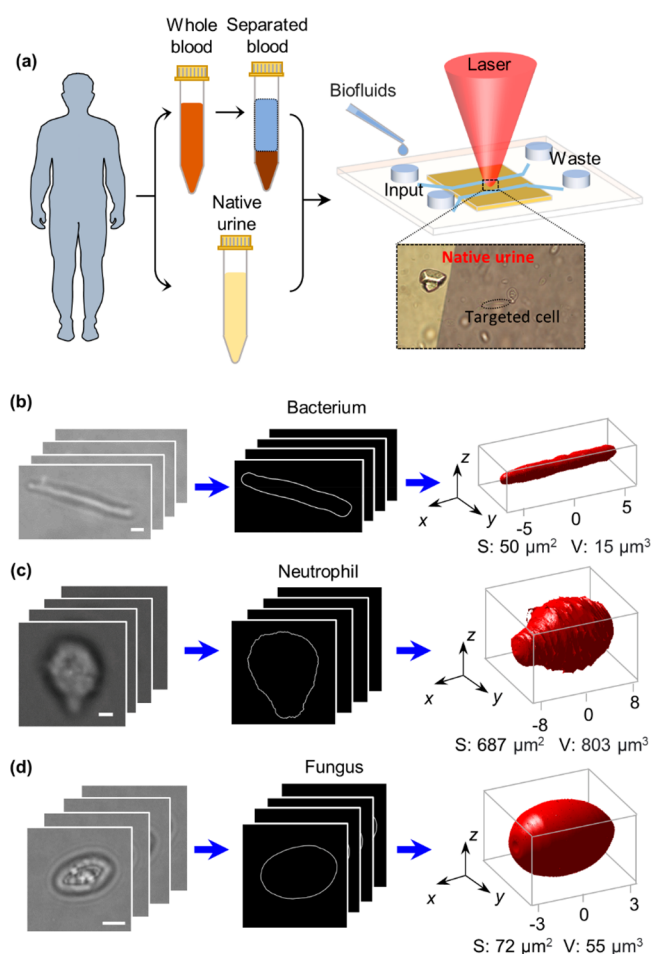


**Figure 3.** General applicability of rotational manipulation for volumetric imaging of organisms in clinical samples. (a) Schematic illustrating the collection and purification of clinical samples and the optical trapping and rotation of targeted biological cells for volumetric imaging. The rotational images (left panel) are extracted to generate the contours (middle panel), which are reconstructed into the 3D surfaces (right panel) for (b) human bacterium, (c) human neutrophil, and (d) human fungus.  $S$  denotes the surface area of the cell and  $V$  the volume of the cell. The scale bars for (b)–(d) are 1, 3, and 2  $\mu\text{m}$ , respectively.

shadowing, occlusion, and scattering with multiangle imaging, our technique can visualize the individual neutrophil microvilli or tethers with a diameter of around 100 nm at the different sites along the neutrophil surface. Therefore, our optical rotation integrated with optical microscopy is instrumental in high-resolution volumetric characterizations of wide-ranging biological samples at the subcellular level.

The ability to acquire optical images from multiple perspectives of individual cells also offers a unique opportunity for ML-based cell identification with high accuracy. Multiangle projection imaging with deterministic angles allows the collection of large numbers of unique images per cell, which can ease the process of data collection for image identification. By rotating cells in an out-of-plane fashion, our platform can record a series of cell images with each projection angle offering slight differences in the orientation of features on and within the cell membranes. With these images as an input data set, our trained ML algorithm can better generalize for predicting the identity of new cells with arbitrary angles relative to the imaging plane (Figure 5). A standard stationary imaging approach, however, needs significantly more cells to be imaged to cover a wide range of samples with variable internal feature orientations required for training ML algorithm to generalize to identify new data. Labeled data collection time is often one of the most significant bottlenecks in ML image recognition tasks.<sup>36</sup> A multiangle projection approach based on optical rotation can collect images far faster and provide viable data sets with small numbers of different cells, offering a significant utility in studying rare cells.

We demonstrate the advantage of our imaging platform in ML applications by training ML algorithms for cell identification on different data sets (Figure 5). One data set was collected with our multiangle projection imaging on rotating cells where a small number of cells was used with multiple-angle images per cell. A second data set was collected from a higher number of cells imaged with a stationary method, leading to one image for each cell. We utilized a convolutional neural network (CNN) to train an image recognition algorithm to differentiate between pathogenic fungus cells (*Candida albicans*: CA) and nonpathogenic fungus cells (*Saccharomyces cerevisiae*: SC) (Figure 5a), which show similar volumetric geometries (Figure S5).<sup>43</sup> The structure of

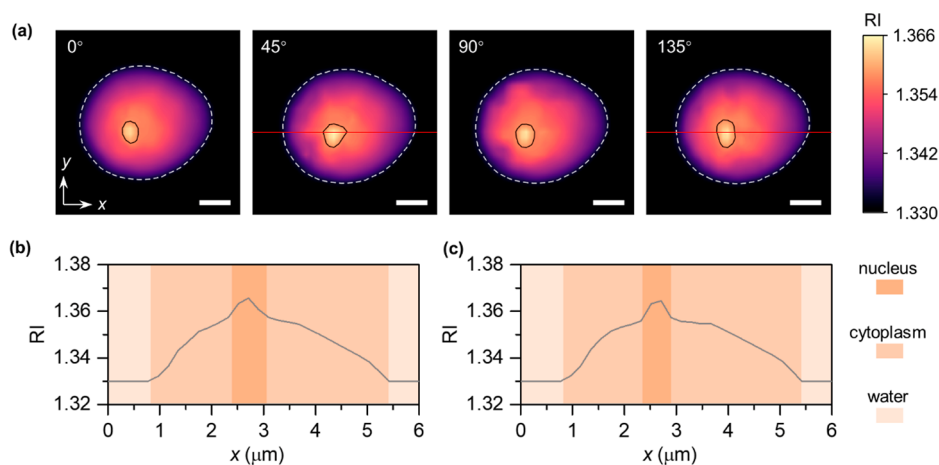


**Figure 4.** Refractive index (RI) mapping of a yeast cell. (a) Image sequence showing refractive index images of a yeast cell at different angles. The dashed white line indicates the boundary of the cell. The black line indicates the boundary of the nucleus. Scale bar: 1  $\mu\text{m}$ . Refractive index values along the red lines in the images in (a) with angles of 45° (b) and 135° (c).

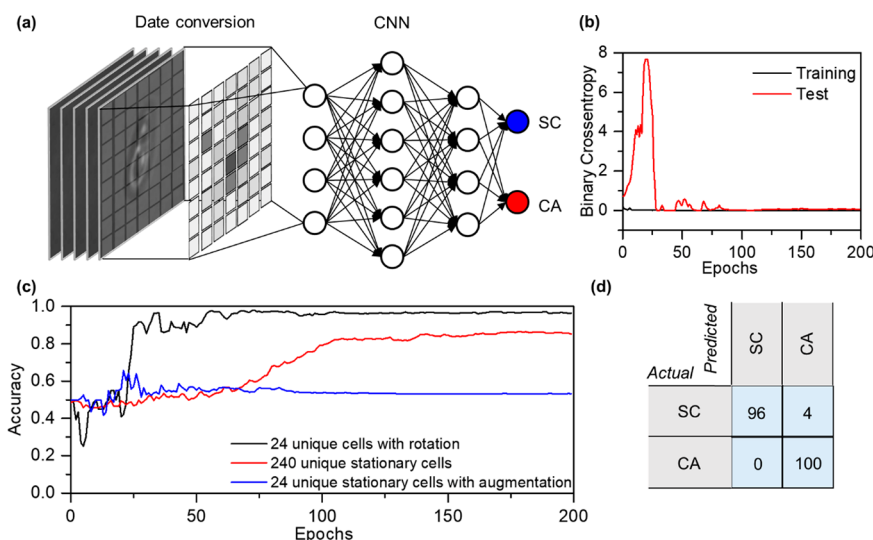


**Figure 5.** Comparison of ML image recognition results using rotation-enabled multiangle imaging and stationary imaging. (a) Schematic of convolutional neural network used to differentiate between cell images. (b) Loss curve over 200 epochs for a model trained with rotational data. (c) Comparison of test set accuracy curves for three data sets. The first data set features 25 rotational images collected for each of 24 unique cells (black). The second uses 240 unique cells with a stationary image for each (red). The final data set uses 24 unique stationary images expanded to the same size as the first data set with traditional image augmentation (blue). For each data set, the number of unique cells refers to the total number across the training and test sets. Each training curve is an average of 10 models. (d) Confusion matrix for the rotational model, with the model prediction rates for SC and CA cells compared with the true cell classifications.

the CNN utilized multiple layers of convolution and max pooling to break down each image into a series of useful features.<sup>44</sup> A final fully connected layer mapped these features into the predicted cell classes.<sup>45</sup> The full architecture is given in Figure S6 in the the Supporting Information.

A loss curve for a single model trained on the multiangle set is shown in Figure 5b. The loss sees an initial large rise in early epochs, likely due to variance and instability from the relatively small data set, before eventually decreasing to a low, consistent value with minimal overfitting from the training loss. To address any potential instability, 10 models for each data set are trained to average the results. Overall, we find that models trained on the multiangle set consistently outperform those trained on the stationary data, despite the stationary set using 10 times the number of cells (i.e., 24 cells vs. 240 cells) (Figure 5c). As also shown in Figure 5c, the multiangle set reaches an average of 96% accuracy on test data (black curve), while the stationary set converges to an accuracy rate of 85% (red curve). A confusion matrix analysis of the multiangle model predictions is shown in Figure 5d.

Lastly, we demonstrate that multiangle projection imaging with optical rotation surpasses traditional image augmentation methods in ML. With the traditional methods, image data sets can have their size inflated by using in-plane rotations, translations, and mirror inversions of the relevant objects within the frame to generate new images<sup>46–48</sup> (Figure S7). All these changes cannot, however, replicate the differences in orientation of internal cell features that adjusting the rotation angle can reveal. We constructed a third data set using a limited set of 12 unique stationary image cells for each type and augmented to a total data set size of 600, which was the same as the original multiangle projection set. To offer the strongest point of comparison, the data augmentations were limited to just in-plane rotations, as additional types of image manipulation for the augmentations weakened the predictive power of the model. We averaged 10 trained models on this

data set. The results show that traditional augmentation techniques cannot compensate for a small initial sample, as the augmented data set only reaches a test accuracy of 53% (blue curve in Figure 5c), only marginally higher than a model making a random guess. We further trained the same model on data sets by varying the number of unique stationary cell images and found a consistent trend that, even using traditional augmentation techniques, the model prediction accuracy rises with the higher number of unique cells (Figure S8). Using the full 240 unique images as well as augmentation to give a total data set size of 600 images, the same as the multiangle set, the resulting trained model gives a prediction accuracy of 91%, slightly less than the 96% accuracy achieved with the multiangle data that uses only 24 unique cells.

In summary, optothermal rotation integrated into optical microscopy opens new opportunities for volumetric imaging and classification of organisms. High-speed rotation of organisms with precise control of their orientations offers multiangle imaging projection that is capable of rapidly acquiring volumetric data at high resolution. In contrast to previous optical rotation methods using shaped laser beams, our optothermal method is applicable to a wide range of organisms in clinical samples. The multiangle projection imaging based on the optothermal rotation can generate sufficient data sets from a small number of unique cells for ML training and enhanced classification of organisms using one-tenth the number of training samples. Since the rotation occurs on organisms near the substrate (with  $\sim 10$  nm gap), emerging characterization methods based on near-field effects (i.e., total internal reflection fluorescence microscopy<sup>5</sup> and plasmon-enhanced phase microscopy<sup>49</sup>) can be readily applied to fully profile single organisms, pushing the frontiers of cellular biology. With ML-assisted organism identification and classification, our technique will also enhance detection of rare pathogenic cells and disease diagnosis.<sup>50,51</sup> In addition, by incorporating super-resolution optical imaging and spectroscopy

copy with optical rotation and ML, we could achieve a higher level of precision and detail in our biochemical and biophysical analysis, leading to a more comprehensive understanding of the complex biological processes taking place at the cellular level.<sup>52</sup>

## ■ ASSOCIATED CONTENT

### SI Supporting Information

The Supporting Information is available free of charge at: . The Supporting Information is available free of charge at <https://pubs.acs.org/doi/10.1021/acs.nanolett.3c01077>.

Optical rotation of single bacterium (MP4)

Optical trapping and rotation of single yeast (MP4)

Optical trapping and rotation of single organism in human urine (MP4)

Volumetric imaging of single bacterium (AVI)

Volumetric imaging of single neutrophil (AVI)

Volumetric imaging of single yeast (AVI)

Materials and methods, measured  $x$ – $y$  plane temperature profiles at the focal point of a 780 nm laser beam directed onto a light-absorbing substrate, force analysis of an optothermally trapped cell with two laser beams, optical rotation of various types of organisms in clinical samples, optical rotation of a small bacterium with a dimension of 300 nm  $\times$  500 nm, statistical analysis of cell sizes, visualization of convolutional neural network architecture used for cell identification, examples of augmented image data created from optical images of single cells captured with stationary methods, comparison of single models trained on stationary data with differing total numbers of unique cells, and the resulting prediction accuracy on test data (PDF)

## ■ AUTHOR INFORMATION

### Corresponding Author

**Yuebing Zheng** – Chandra Department of Electrical and Computer Engineering, The University of Texas at Austin, Austin, Texas 78712, United States; Walker Department of Mechanical Engineering, Materials Science & Engineering Program and Texas Materials Institute, and Department of Biomedical Engineering, The University of Texas at Austin, Austin, Texas 78712, United States; [orcid.org/0000-0002-9168-9477](https://orcid.org/0000-0002-9168-9477); Email: [zheng@austin.utexas.edu](mailto:zheng@austin.utexas.edu)

### Authors

**Yaoran Liu** – Chandra Department of Electrical and Computer Engineering, The University of Texas at Austin, Austin, Texas 78712, United States

**Rohit Unni** – Walker Department of Mechanical Engineering and Materials Science & Engineering Program and Texas Materials Institute, The University of Texas at Austin, Austin, Texas 78712, United States

**Xin Lou** – School of Physical Sciences, University of Chinese Academy of Sciences, Beijing 100049, People's Republic of China; Wenzhou Institute, University of Chinese Academy of Sciences, Wenzhou, Zhejiang 325001, China

**Mingcheng Yang** – School of Physical Sciences, University of Chinese Academy of Sciences, Beijing 100049, People's Republic of China; Beijing National Laboratory for Condensed Matter Physics and Laboratory of Soft Matter Physics, Institute of Physics, Chinese Academy of Sciences, Beijing 100190, People's Republic of China; Songshan Lake

Materials Laboratory, Dongguan, Guangdong 523808, People's Republic of China

Complete contact information is available at: <https://pubs.acs.org/doi/10.1021/acs.nanolett.3c01077>

### Author Contributions

Y.L. and R.U. contributed equally to this work.

### Notes

The authors declare no competing financial interest.

## ■ ACKNOWLEDGMENTS

Y.L., R.U., and Y.Z. acknowledge the financial support of the National Institute of General Medical Sciences of the National Institutes of Health (1R01GM146962-01) and National Science Foundation (ECCS-2001650). X.L. and M.Y. acknowledge the financial support of the National Natural Science Foundation of China (No. 11874397).

## ■ REFERENCES

- (1) Monks, C. R.; Freiberg, B. A.; Kupfer, H.; Sciaky, N.; Kupfer, A. Three-dimensional segregation of supramolecular activation clusters in T cells. *Nature* **1998**, *395* (6697), 82–86.
- (2) Wu, W.; Singh, M.; Masud, A.; Wang, X.; Nallapaneni, A.; Xiao, Z.; Zhai, Y.; Wang, Z.; Terlier, T.; Bleuel, M.; Yuan, G.; Satija, S. K.; Douglas, J. F.; Matyjaszewski, K.; Bockstaller, M. R.; Karim, A. Control of Phase Morphology of Binary Polymer Grafted Nanoparticle Blend Films via Direct Immersion Annealing. *ACS Nano* **2021**, *15* (7), 12042–12056.
- (3) Swoger, J.; Verveer, P.; Greger, K.; Huisken, J.; Stelzer, E. H. Multi-view image fusion improves resolution in three-dimensional microscopy. *Opt. Express* **2007**, *15* (13), 8029–8042.
- (4) Huisken, J.; Swoger, J.; Del Bene, F.; Wittbrodt, J.; Stelzer, E. H. Optical sectioning deep inside live embryos by selective plane illumination microscopy. *Science* **2004**, *305* (5686), 1007–1009.
- (5) Axelrod, D. Total internal reflection fluorescence microscopy in cell biology. *Traffic* **2001**, *2* (11), 764–774.
- (6) Power, R. M.; Huisken, J. A guide to light-sheet fluorescence microscopy for multiscale imaging. *Nat. Methods* **2017**, *14* (4), 360–373.
- (7) He, J.; Huisken, J. Image quality guided smart rotation improves coverage in microscopy. *Nat. Commun.* **2020**, *11* (1), 1–9.
- (8) Chang, B.-J.; Manton, J. D.; Sapoznik, E.; Pohlkamp, T.; Terrones, T. S.; Welf, E. S.; Murali, V. S.; Roudot, P.; Hake, K.; Whitehead, L.; et al. Real-time multi-angle projection imaging of biological dynamics. *Nat. Methods* **2021**, *18* (7), 829–834.
- (9) Calisesi, G.; Candeo, A.; Farina, A.; D'Andrea, C.; Magni, V.; Valentini, G.; Pistocchi, A.; Costa, A.; Bassi, A. Three-dimensional bright-field microscopy with isotropic resolution based on multi-view acquisition and image fusion reconstruction. *Sci. Rep.* **2020**, *10* (1), 1–9.
- (10) Chhetri, R. K.; Amat, F.; Wan, Y.; Höckendorf, B.; Lemon, W. C.; Keller, P. J. Whole-animal functional and developmental imaging with isotropic spatial resolution. *Nat. Methods* **2015**, *12* (12), 1171–1178.
- (11) Ahmed, D.; Ozelik, A.; Bojanala, N.; Nama, N.; Upadhyay, A.; Chen, Y.; Hanna-Rose, W.; Huang, T. J. Rotational manipulation of single cells and organisms using acoustic waves. *Nat. Commun.* **2016**, *7* (1), 1–11.
- (12) Tang, T.; Hosokawa, Y.; Hayakawa, T.; Tanaka, Y.; Li, W.; Li, M.; Yalikul, Y. Rotation of biological cells: fundamentals and applications. *Engineering* **2022**, *10*, 110.
- (13) Ding, X.; Lin, S.-C. S.; Kiraly, B.; Yue, H.; Li, S.; Chiang, I.-K.; Shi, J.; Benkovic, S. J.; Huang, T. J. On-chip manipulation of single microparticles, cells, and organisms using surface acoustic waves. *Proc. Natl. Acad. Sci. U. S. A.* **2012**, *109* (28), 11105–11109.

- (14) Ding, X.; Li, P.; Lin, S.-C. S.; Stratton, Z. S.; Nama, N.; Guo, F.; Slotcavage, D.; Mao, X.; Shi, J.; Costanzo, F.; et al. Surface acoustic wave microfluidics. *Lab Chip* **2013**, *13* (18), 3626–3649.
- (15) Läubli, N. F.; Burri, J. T.; Marquard, J.; Vogler, H.; Mosca, G.; Vertti-Quintero, N.; Shamsudhin, N.; DeMello, A.; Grossniklaus, U.; Ahmed, D.; et al. 3D mechanical characterization of single cells and small organisms using acoustic manipulation and force microscopy. *Nat. Commun.* **2021**, *12* (1), 1–11.
- (16) Shen, K.; Duan, Y.; Ju, P.; Xu, Z.; Chen, X.; Zhang, L.; Ahn, J.; Ni, X.; Li, T. On-chip optical levitation with a metalens in vacuum. *Optica* **2021**, *8* (11), 1359–1362.
- (17) Ashkin, A.; Dziedzic, J. M.; Yamane, T. Optical trapping and manipulation of single cells using infrared laser beams. *Nature* **1987**, *330* (6150), 769–771.
- (18) Maragò, O. M.; Jones, P. H.; Gucciardi, P. G.; Volpe, G.; Ferrari, A. C. Optical trapping and manipulation of nanostructures. *Nature Nanotechnol.* **2013**, *8* (11), 807–819.
- (19) Pang, Y.; Gordon, R. Optical trapping of a single protein. *Nano Lett.* **2012**, *12* (1), 402–406.
- (20) Pang, Y.; Song, H.; Kim, J. H.; Hou, X.; Cheng, W. Optical trapping of individual human immunodeficiency viruses in culture fluid reveals heterogeneity with single-molecule resolution. *Nature Nanotechnol.* **2014**, *9* (8), 624–630.
- (21) Ndukaife, J. C.; Kildishev, A. V.; Nnanna, A. G. A.; Shalae, V. M.; Wereley, S. T.; Boltasseva, A. Long-range and rapid transport of individual nano-objects by a hybrid electrothermoplasmonic nanotweezer. *Nature Nanotechnol.* **2016**, *11* (1), 53–59.
- (22) Stilgoe, A. B.; Nieminen, T. A.; Rubinsztein-Dunlop, H. Controlled transfer of transverse orbital angular momentum to optically trapped birefringent microparticles. *Nat. Photonics* **2022**, *16*, 346–351.
- (23) Sudhakar, S.; Abdosamadi, M. K.; Jachowski, T. J.; Bugiel, M.; Jannasch, A.; Schäffer, E. Germanium nanospheres for ultraresolution picotensiometry of kinesin motors. *Science* **2021**, *371* (6530), No. eabd9944.
- (24) Moffitt, J. R.; Chemla, Y. R.; Smith, S. B.; Bustamante, C. Recent advances in optical tweezers. *Annu. Rev. Biochem.* **2008**, *77*, 205–228.
- (25) Avsievich, T.; Zhu, R.; Popov, A.; Bykov, A.; Meglinski, I. The advancement of blood cell research by optical tweezers. *Reviews in Physics* **2020**, *5*, 100043.
- (26) Arzola, A. V.; Ják, P.; Chvátal, L.; Zemánek, P. Rotation, oscillation and hydrodynamic synchronization of optically trapped oblate spheroidal microparticles. *Opt. Express* **2014**, *22* (13), 16207–16221.
- (27) Schürmann, M.; Cojoc, G.; Girardo, S.; Ulbricht, E.; Guck, J.; Müller, P. Three-dimensional correlative single-cell imaging utilizing fluorescence and refractive index tomography. *Journal of biophotonics* **2018**, *11* (3), No. e201700145.
- (28) Jünger, F.; Ruh, D.; Strobel, D.; Michiels, R.; Huber, D.; Brandl, A.; Madl, J.; Gavrilov, A.; Mihlan, M.; Daller, C. C.; et al. 100 Hz ROCS microscopy correlated with fluorescence reveals cellular dynamics on different spatiotemporal scales. *Nat. Commun.* **2022**, *13* (1), 1–17.
- (29) Sun, J.; Koukourakis, N.; Guck, J.; Czarske, J. W. Rapid computational cell-rotation around arbitrary axes in 3D with multi-core fiber. *Biomedical Optics Express* **2021**, *12* (6), 3423–3437.
- (30) Aiello, A.; Banzer, P.; Neugebauer, M.; Leuchs, G. From transverse angular momentum to photonic wheels. *Nat. Photonics* **2015**, *9* (12), 789–795.
- (31) Moen, E.; Bannon, D.; Kudo, T.; Graf, W.; Covert, M.; Van Valen, D. Deep learning for cellular image analysis. *Nat. Methods* **2019**, *16* (12), 1233–1246.
- (32) Xing, F.; Xie, Y.; Su, H.; Liu, F.; Yang, L. Deep Learning in Microscopy Image Analysis: A Survey. *IEEE Transactions on Neural Networks and Learning Systems* **2018**, *29* (10), 4550–4568.
- (33) Caicedo, J. C.; Cooper, S.; Heigwer, F.; Warchal, S.; Qiu, P.; Molnar, C.; Vasilevich, A. S.; Barry, J. D.; Bansal, H. S.; Kraus, O.; Wawer, M.; Paavolainen, L.; Herrmann, M. D.; Rohban, M.; Hung, J.; Hennig, H.; Concannon, J.; Smith, I.; Clemons, P. A.; Singh, S.; Rees, P.; Horvath, P.; Lington, R. G.; Carpenter, A. E. Data-analysis strategies for image-based cell profiling. *Nat. Methods* **2017**, *14* (9), 849–863.
- (34) Kraus, O. Z.; Ba, J. L.; Frey, B. J. Classifying and segmenting microscopy images with deep multiple instance learning. *Bioinformatics* **2016**, *32* (12), i52–i59.
- (35) Godinez, W. J.; Hossain, I.; Lazic, S. E.; Davies, J. W.; Zhang, X. A multi-scale convolutional neural network for phenotyping high-content cellular images. *Bioinformatics* **2017**, *33* (13), 2010–2019.
- (36) Caicedo, J. C.; Roth, J.; Goodman, A.; Becker, T.; Karhohs, K. W.; Broisin, M.; Molnar, C.; McQuinn, C.; Singh, S.; Theis, F. J.; Carpenter, A. E. Evaluation of Deep Learning Strategies for Nucleus Segmentation in Fluorescence Images. *Cytometry A* **2019**, *95* (9), 952–965.
- (37) Lin, L.; Peng, X.; Mao, Z.; Li, W.; Yogeesh, M. N.; Rajeeva, B. B.; Perillo, E. P.; Dunn, A. K.; Akinwande, D.; Zheng, Y. Bubble-pen lithography. *Nano Lett.* **2016**, *16* (1), 701–708.
- (38) Lin, L.; Wang, M.; Peng, X.; Lissek, E. N.; Mao, Z.; Scarabelli, L.; Adkins, E.; Coskun, S.; Unalan, H. E.; Korgel, B. A.; et al. Opto-thermoelectric nanotweezers. *Nat. Photonics* **2018**, *12* (4), 195–201.
- (39) Braun, M.; Cichos, F. Optically controlled thermophoretic trapping of single nano-objects. *ACS Nano* **2013**, *7* (12), 11200–11208.
- (40) Bregulla, A. P.; Würger, A.; Günther, K.; Mertig, M.; Cichos, F. Thermo-osmotic flow in thin films. *Physical review letters* **2016**, *116* (18), 188303.
- (41) Fu, L.; Merabia, S.; Joly, L. What controls thermo-osmosis? Molecular simulations show the critical role of interfacial hydrodynamics. *Physical review letters* **2017**, *119* (21), 214501.
- (42) Lou, X.; Yu, N.; Liu, R.; Chen, K.; Yang, M. Dynamics of a colloidal particle near a thermosmotic wall under illumination. *Soft Matter* **2018**, *14* (8), 1319–1326.
- (43) Calderone, R. A.; Fonzi, W. A. Virulence factors of *Candida albicans*. *Trends in microbiology* **2001**, *9* (7), 327–335.
- (44) Krizhevsky, A.; Sutskever, I.; Hinton, G. E., ImageNet classification with deep convolutional neural networks. In *Proceedings of the 25th International Conference on Neural Information Processing Systems*; Curran Associates Inc.: 2012; Vol. 1, pp 1097–1105.
- (45) Basha, S. H. S.; Dubey, S. R.; Pulabaigari, V.; Mukherjee, S. Impact of fully connected layers on performance of convolutional neural networks for image classification. *Neurocomputing* **2020**, *378*, 112–119.
- (46) Shorten, C.; Khoshgoftaar, T. M. A survey on Image Data Augmentation for Deep Learning. *Journal of Big Data* **2019**, *6* (1), 60.
- (47) Cireşan, D. C.; Meier, U.; Gambardella, L. M.; Schmidhuber, J. Deep, Big, Simple Neural Nets for Handwritten Digit Recognition. *Neural Computation* **2010**, *22* (12), 3207–3220.
- (48) Helgadottir, S.; Midtvedt, B.; Pineda, J.; Sabirsh, A.; B. Adiels, C.; Romeo, S.; Midtvedt, D.; Volpe, G. Extracting quantitative biological information from bright-field cell images using deep learning. *Biophysics Reviews* **2021**, *2* (3), 031401.
- (49) Balaur, E.; Cadenazzi, G. A.; Anthony, N.; Spurling, A.; Hanssen, E.; Orian, J.; Nugent, K. A.; Parker, B. S.; Abbey, B. Plasmon-induced enhancement of ptychographic phase microscopy via sub-surface nanoaperture arrays. *Nat. Photonics* **2021**, *15* (3), 222–229.
- (50) Zhong, M.-C.; Wei, X.-B.; Zhou, J.-H.; Wang, Z.-Q.; Li, Y.-M. Trapping red blood cells in living animals using optical tweezers. *Nat. Commun.* **2013**, *4* (1), 1–7.
- (51) Brandao, M.; Fontes, A.; Barjas-Castro, M.; Barbosa, L.; Costa, F.; Cesar, C.; Saad, S. Optical tweezers for measuring red blood cell elasticity: application to the study of drug response in sickle cell disease. *European journal of haematology* **2003**, *70* (4), 207–211.
- (52) Yao, K.; Zheng, Y. *Nanophotonics and Machine Learning*; 1st ed.; Springer: 2023; Vol. 1, pp 1–178. DOI: 10.1007/978-3-031-20473-9.